A Single-Atom-Thick TiO_2 Nanomesh on an Insulating Oxide

Takeo Ohsawa,*,†,‡ Mitsuhiro Saito,†,¶ Ikutaro Hamada,†,‡ Ryota Shimizu,† Katsuya Iwaya,† Susumu Shiraki,† Zhongchang Wang,† Yuichi Ikuhara,†,¶,§ and Taro Hitosugi*,†,∥

†Advanced Institute for Materials Research (AIMR), Tohoku University, Sendai 980-8577, Japan, ‡National Institute for Materials Science (NIMS), 1-1 Namiki, Tsukuba 305-0044, Japan, ¶Institute of Engineering Innovation, The University of Tokyo, Tokyo, 113-8656, Japan, §Nanostructures Research Laboratory, Japan Fine Ceramics Center, Nagoya, 456-8587, Japan, and ∥PRESTO, Japan Science and Technology Agency, Tokyo 102-0076, Japan

ABSTRACT The electronic structures and macroscopic functionalities of two-dimensional (2D) materials are often controlled according to their size, atomic structures, and associated defects. This controllability is particularly important in ultrathin 2D nanosheets of transition-metal oxides because these materials exhibit extraordinary multifunctionalities that cannot be realized in their bulk constituents. To expand the variety of materials with exotic properties that can be used in 2D transition-metal-oxide nanosheets, it is essential to investigate fabrication processes for 2D materials. However, it remains challenging to fabricate such 2D nanosheets, as they are often forbidden because of the crystal structure and nature of their host oxides. In this study, we demonstrate the synthesis of a single-atom-thick TiO_2 2D nanosheet with a periodic array of holes, that is, a TiO_2 nanomesh, by depositing a $LaAlO_3$ thin film on a $SrTiO_3(001)$-$(\sqrt{13}\times\sqrt{13})$-*R*33.7° reconstructed substrate. In-depth investigations of the detailed structures, local density of states, and Ti valency of the TiO_2 nanomesh using scanning tunneling microscopy/spectroscopy, scanning transmission electron microscopy, and density functional theory calculations reveal an unexpected upward migration of the Ti atoms of the substrate surface onto the $LaAlO_3$ surface. These results indicate that the truncated TiO_5 octahedra on the surface of perovskite oxides are very stable, leading to semiconducting TiO_2 nanomesh formation. This nanomesh material can be potentially used to control the physical and chemical properties of the surfaces of perovskite oxides. Furthermore, this study provides an avenue for building functional atomic-scale oxide 2D structures and reveals the thin-film growth processes of complex oxides.

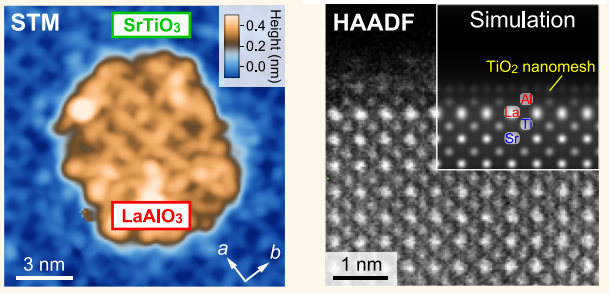

KEYWORDS: two-dimensional sheets · transition metal oxides · strontium titanate · lanthanum aluminate · scanning tunneling microscopy

When layered materials are thinned into two-dimensional (2D) nanosheets one or a few atoms in thickness, such as graphene or metal dichalcogenide sheets, extraordinary electronic, optical, and mechanical properties emerge.[1−3] Among 2D materials, transition-metal-oxide (TMO) 2D nanosheets have attracted significant attention,[4−6] because of the multifunctionalities of TMOs, including catalysis,[7] the colossal magnetoresistive effect,[8] and superconducting properties.[9] In addition to the fabrication of TMO nanosheets, considerable effort has been devoted to modify their size, shape, and edge atomic structures, with the aim of discovering new functionalities, as is demonstrated in the tuning of the band gap, luminescence, and magnetic properties of graphene by adjusting its size[10] and edge structures.[11] Such structural control enables the tuning of fundamental physical and chemical properties, allowing a wide range of advanced device applications based on TMO 2D sheets. Although many TMO materials can theoretically be prepared as 2D sheets, the number of oxides with single-atom thickness is actually quite limited. This is because the fabrication processes, that is, deposition and exfoliation, rely on not only crystal structures but also the chemical properties of the host compound. Therefore, the development of new techniques to fabricate single-atom-thick 2D TMOs is essential to explore the variety of TMO 2D sheets.

Titania (TiO_2) in the form of nanoparticles, nanotubes, and nanoporous structures is of great interest for photocatalysis, solar cells, and water splitting.[12] Moreover, TiO_2 nanosheets have attracted considerable attention because they exhibit substantial

* Address correspondence to ohsawa.takeo@nims.go.jp, hitosugi@wpi-aimr.tohoku.ac.jp.

Received for review March 8, 2015 and accepted August 8, 2015.

Published online August 20, 2015
10.1021/acsnano.5b02867

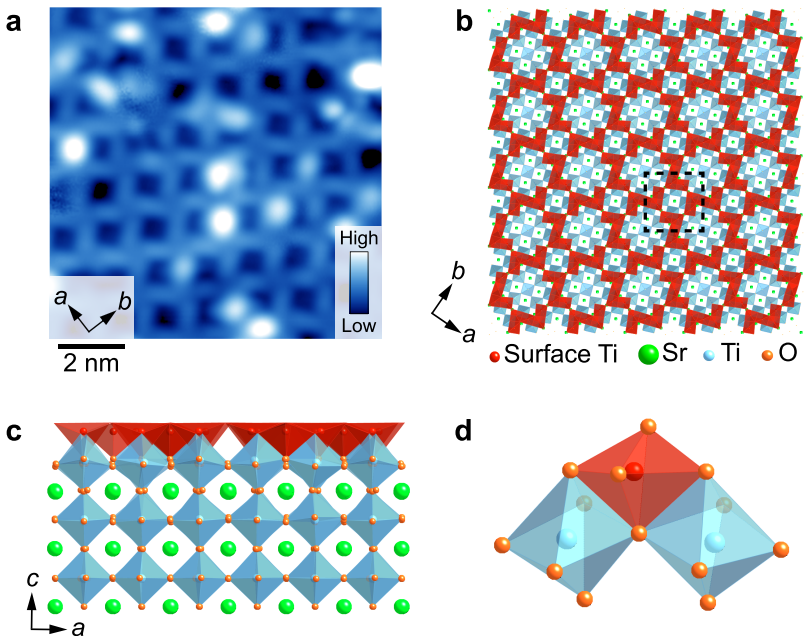

Figure 1. (a) An STM image of the $SrTiO_3$(001)-($\sqrt{13}\times\sqrt{13}$)-*R*33.7° surface (V_s = +1.2 V, I_t = 30 pA, 10 × 10 nm^2). (b) Top view and (c) side view of the surface structure. Surface Ti atoms and bulk Sr, Ti, and O atoms in $SrTiO_3$ are represented in red, green, light blue, and orange, respectively. The broken square in panel b indicates the unit cell of $SrTiO_3$(001)-($\sqrt{13}\times\sqrt{13}$)-*R*33.7°. The blue and red polyhedrals in panel c show the TiO_6 octahedra and truncated TiO_5 at the surface, respectively. (d) A close-up view of the truncated TiO_5 octahedral unit (red) that forms the two-dimensional network at the surface.

promise as gate insulators, semiconductors, and conductors owing to the precise control of their chemical composition. Despite intensive efforts toward the fabrication of TiO_2 nanostructures,[4−6] basic knowledge regarding the well-defined synthesis of single-atom-thick TiO_2 2D nanosheets with controllable lateral shapes and defined edge structures at the atomic scale has yet to be established.

We synthesized a single-atom-thick TiO_2 nanomesh with a periodic array of circular holes (diameters of ~1 nm and ~0.6 nm) on an insulating $LaAlO_3/SrTiO_3$ heterostructure. This was achieved by a combination of scanning tunneling microscopy (STM) and pulsed laser deposition (PLD) systems,[13] which enabled us to observe the clean surfaces of oxide thin films without exposure to air after deposition.[14,15] The fabrication of the single-atom-thick TiO_2 2D nanomesh involved the surface structure of a $SrTiO_3$ substrate and the initial growth process of $LaAlO_3$ thin films. Upon closer inspection by STM, scanning tunneling spectroscopy (STS), and scanning transmission electron microscopy (STEM), we found that a TiO_2 2D nanomesh spontaneously detached from the original $SrTiO_3$ surface and then recrystallized on top of the AlO_2 layer of $LaAlO_3$. The 2D nanomesh adopted an electrically semiconducting nature with a valence state of Ti^{4+}. We further revealed that the stability of truncated TiO_5 octahedra on the perovskite surface was the driving force behind the formation of the single-atom-thick TiO_2 nanomesh. These processes indicate that a 2D TiO_2 nanomesh can be grown uniformly over other perovskite oxides, as we demonstrated using STEM. This study paves the way to expand the variations of oxide 2D materials, which should affect a variety of fields, including catalysis, sensing, and electronic devices.

RESULTS AND DISCUSSION

We first discuss the atomic arrangement and electronic structure of the $SrTiO_3$(001)-($\sqrt{13}\times\sqrt{13}$)-*R*33.7° reconstructed substrate surface. Figure 1a shows a typical STM image, taken at a sample bias voltage (V_s) of +1.2 V, of a reconstructed substrate surface before the deposition of the $LaAlO_3$ film. The STM image shows a periodic pattern comprising large and small dark squares separated by bright lines, which can be explained by the double-layer model, that is, a TiO_2 layer on a TiO_2-terminated $SrTiO_3$(001) substrate surface.[16−19] Truncated octahedra of TiO_5 form a two-dimensional network by sharing their edges with TiO_6 octahedra underneath (Figure 1b−d), as discussed later. This reconstructed surface is stable under the typical deposition conditions needed to grow the oxide thin films and is hence considered suitable for studying the growth process of oxide films.[20−22]

Prior to the epitaxial growth of $LaAlO_3$ for STM measurements, we optimized the growth conditions of the $LaAlO_3$ epitaxial films on the $SrTiO_3$ substrates. The growth of $LaAlO_3$ films was monitored *in situ* using reflection high-energy electron diffraction (RHEED) intensity oscillations. Figure 2a shows that layer-by-layer growth of $LaAlO_3$ films on the $SrTiO_3$(001)-($\sqrt{13}\times\sqrt{13}$)-*R*33.7° substrates were attained under

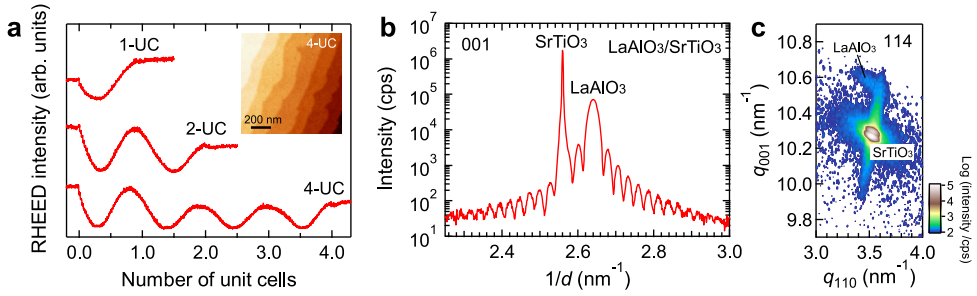

Figure 2. (a) RHEED intensity oscillations of the specular reflected beam for the $LaAlO_3$ growth on the $SrTiO_3$(001)-($\sqrt{13}\times\sqrt{13}$)-*R*33.7° substrates. The inset shows an AFM image of a 4-UC-thick $LaAlO_3$ film (image size: 1 μm × 1 μm). (b) High-resolution XRD in the vicinity of the 001 $LaAlO_3$ and $SrTiO_3$ reflections for a 100-UC-thick $LaAlO_3$ thin film. (c) Reciprocal space mapping in the vicinity of the 114 reflection of the $LaAlO_3/SrTiO_3$ sample in panel b. q is the scattering vector expressed as $q = (2/\lambda)\sin\theta$, where λ is the X-ray wavelength (Cu Kα, 1.5418 Å), and θ is the angle of X-ray incidence with respect to the surface of thin-film growth.

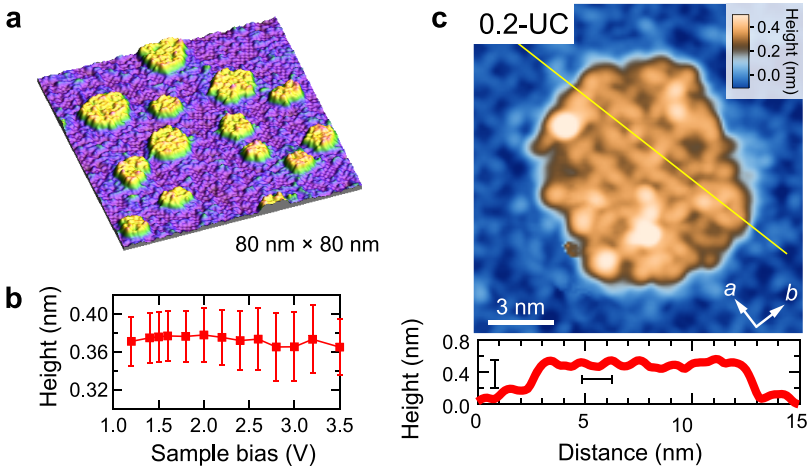

Figure 3. (a) A wide-area STM image of 0.2-UC $LaAlO_3$ islands on the $SrTiO_3$(001)-($\sqrt{13}\times\sqrt{13}$)-*R*33.7° surface (V_s = +3.5 V, I_t = 30 pA, 80 × 80 nm^2). (b) Bias dependence of height of $LaAlO_3$ islands. (c) An STM image of a 0.2-UC $LaAlO_3$ island (V_s = +1.2 V, I_t = 30 pA, 15 × 15 nm^2).[25] The atomic structure, which is identical to that of the $SrTiO_3$(001)-($\sqrt{13}\times\sqrt{13}$)-*R*33.7° substrate surface, is identified on the $LaAlO_3$ island. Height profile along the yellow line in panel c is shown at the bottom. Vertical and lateral scales correspond to approximately 0.38 and 1.4 nm, respectively. The lateral periodicity of ~1.4 nm matches with that of the ($\sqrt{13}\times\sqrt{13}$)-*R*33.7° reconstruction of $SrTiO_3$.

our growth conditions, and the film thickness was thereby controlled to 1, 2, or 4 unit cells (UC). Moreover, as shown by an atomic force microscope (AFM) image, clear step-and-terrace structures of the 4-UC-thick $LaAlO_3$ film indicate that high-quality $LaAlO_3$ epitaxial films were grown [inset of Figure 2a]. We further grew a 100-UC-thick $LaAlO_3$ film on a $SrTiO_3$(001)-($\sqrt{13}\times\sqrt{13}$)-*R*33.7° substrate and performed a high-resolution X-ray diffraction (XRD) analysis. Figure 2b shows clear and persistent fringes on the 001 $LaAlO_3$ Bragg reflections, which arose from the interference between the $LaAlO_3$ film and the $SrTiO_3$(001)-($\sqrt{13}\times\sqrt{13}$)-*R*33.7° substrate.[23,24] To identify the epitaxial relationship between the $LaAlO_3$ film and $SrTiO_3$(001)-($\sqrt{13}\times\sqrt{13}$)-*R*33.7° substrate, we performed reciprocal space mapping of the film in the vicinity of the 114 peak [Figure 2c]. The in-plane lattice constant of the $LaAlO_3$ film, estimated as $a = \sqrt{2}/q_{110}$, was confirmed to match that of the $SrTiO_3$(001)-($\sqrt{13}\times\sqrt{13}$)-*R*33.7° substrate, indicating a pseudomorphic epitaxial relationship. These experimental results show that our growth conditions are optimized to prepare sufficiently high-quality and smooth $LaAlO_3$ films to conduct STM measurements.

To investigate the atomistic growth processes of epitaxial $LaAlO_3$ thin films on the reconstructed $SrTiO_3$ substrate, we deposited 0.2-UC of $LaAlO_3$ on the reconstructed surface. Figure 3a shows an STM image of the formation of many islands approximately 10 nm in lateral size. The height of the islands was evaluated to be 0.4 nm, which is consistent with the lattice constant (~0.38 nm) of $LaAlO_3$, with negligible V_s dependence between +1.2 and +3.5 V (Figure 3b). Remarkably, an identical square pattern with ($\sqrt{13}\times\sqrt{13}$) periodicity is clearly observed in the magnified image of the $LaAlO_3$ island (Figure 3c).[25]

To chemically identify the observed structure on the $LaAlO_3$ islands, we performed STS measurements of the island shown in Figure 3c (spatial resolution of 128 × 128 pixels for 15 nm × 15 nm). Local-density-of-states

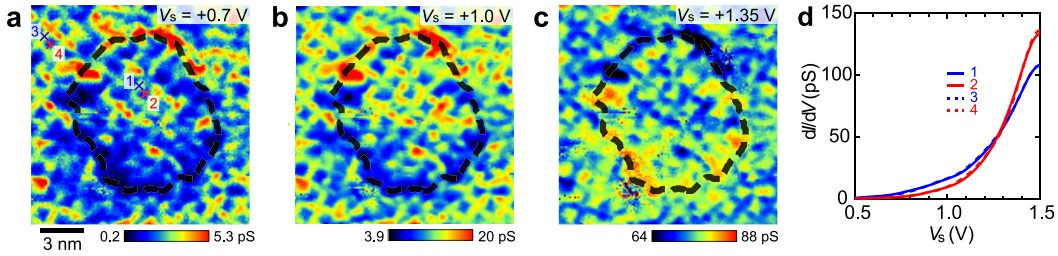

Figure 4. A series of d*I*/d*V* maps of the $LaAlO_3/SrTiO_3$ island taken at a V_s of (a) + 0.7 V, (b) + 1.0 V, and (c) + 1.35 V. The location is exactly the same as that of the STM image in Figure 3c. A negligible difference is observed between the $LaAlO_3$ island and the $SrTiO_3$ substrate. (d) d*I*/d*V* spectra measured at different four sites (1−4) in panel a. The d*I*/d*V* spectra 1 and 2 are observed on the $LaAlO_3$ island surface, while 3 and 4 are observed on the $SrTiO_3$ substrate surface.

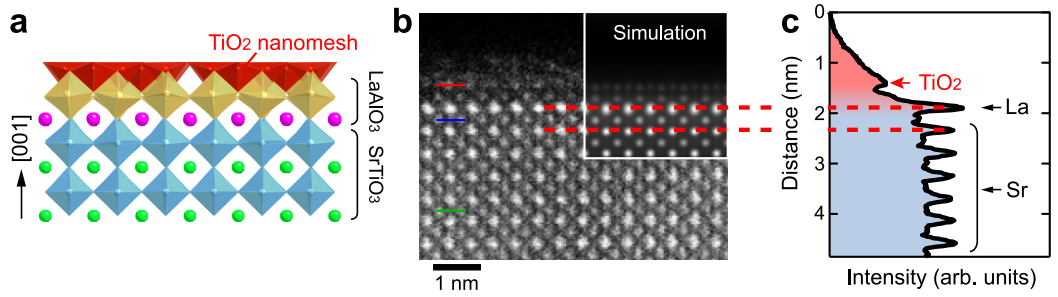

Figure 5. A model of the $LaAlO_3/SrTiO_3$ interface (TiO_2 nanomesh/AlO_2/LaO/bulk TiO_2). The TiO_2 nanomesh [$(\sqrt{13}\times\sqrt{13})$-*R*33.7° structure] of the substrate has migrated onto the surface of the $LaAlO_3$ island. (b) A HAADF STEM image of the 1-UC-thick $LaAlO_3$ on the $SrTiO_3$(001)-$(\sqrt{13}\times\sqrt{13})$-*R*33.7° substrate. A simulation image is shown in the inset. (c) Depth profile along the interface normal.

(LDOS) mapping, d*I*/d*V* mapped with V_s ranging from 0 to +1.5 V (Figure 4a−c), indicated a very similar spatial distribution of the LDOS between the $LaAlO_3$ island surface and the surrounding $SrTiO_3$(001)-$(\sqrt{13}\times\sqrt{13})$-*R*33.7° surface (see the Supporting Information video). Figure 4d shows d*I*/d*V* spectra measured at different four sites in Figure 4a, where 1 and 2 are observed on the $LaAlO_3$ island surface, while 3 and 4 are observed on the $SrTiO_3$ substrate surface. The square pattern observed in both the island and substrate surface (Figures 4a, b) became reversed contrast at V_s = +1.35 V (Figure 4c). Moreover, the intensity of d*I*/d*V* and distribution patterns were comparable between the two surfaces. Because the d*I*/d*V* mapping is highly correlated with the local chemical properties at the surface, it is reasonable to assume that the chemical species on the surface of the $LaAlO_3$ islands and $SrTiO_3$ substrate were identical. A local-barrier-height (LBH) measurement confirmed that the decay rates of the surface-wave functions were quite similar between the $LaAlO_3$ islands and the substrate surface (Figure S1). Both the STS and LBH results strongly suggest that the chemical species on top of the $LaAlO_3$ islands are identical to the TiO_2 nanomesh observed on the $SrTiO_3$-(001)-$(\sqrt{13}\times\sqrt{13})$-*R*33.7° substrate.

In light of these observations, we developed a model for this $LaAlO_3/SrTiO_3$ heterostructure (Figure 5a). In this model, a $LaAlO_3$ monolayer is deposited on the TiO_2-terminated $SrTiO_3$ surface, preserving the AO/BO_2 stacking of the ABO_3 perovskite in the [001] direction. A TiO_2 nanomesh with a periodicity of $(\sqrt{13}\times\sqrt{13})$ is generated on top of the AlO_2 layer, forming the configuration of TiO_2 nanomesh/AlO_2/LaO/TiO_2-terminated $SrTiO_3$.

To verify the formation of the TiO_2 nanomesh on the $LaAlO_3$, we conducted density-functional-theory (DFT) calculations for a TiO_2 nanomesh on top of 1-UC-thick $LaAlO_3$ grown on the TiO_2-terminated $SrTiO_3$ (Figure 5a). In addition, high-angle annular dark-field (HAADF) STEM imaging of the heterostructure in the cross-sectional direction (Figure 5b) was conducted. Because the intensity of an atomic column in the HAADF imaging mode is proportional to $\sim Z^{1.7}$ (*Z*: atomic number), the contrast is bright for heavy atoms in the atomic columns.[26] Therefore, the brightest spots in the monolayer represent LaO columns, whereas the second- and third-brightest spots represent SrO and TiO_2 columns, respectively. This corroborates the presence of a LaO monolayer on top of the bulk-TiO_2 layer. Such a stacking configuration is confirmed by the intensity line profile obtained along the interface normal (Figure 5c), which exhibits a strong peak corresponding to the LaO column (marked by an arrow), along with relatively weaker SrO and TiO_2 peaks. Interestingly, there appear to be two layers on top of the LaO layer (Figure 5b,c). The darker layer directly on top of the LaO layer is AlO_2 (considering the ABO_3 stacking), whereas the slightly brighter topmost layer is the TiO_2 nanomesh uniformly formed on the surface. These two layers can also be identified in the annular bright-field (ABF) STEM image

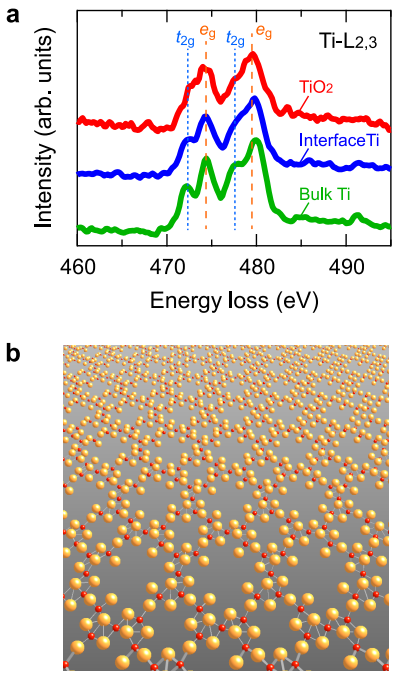

Figure 6. ELNES of the Ti-$L_{2,3}$ edges measured at bulk (green), interface (blue), and topmost surfaces (red). The colors correspond to the layers in Figure 5b. (b) A schematic of TiO_2 nanomesh (Ti: red, O: orange) formed on $LaAlO_3$. Note that periodic holes are present in the single-atom-thick sheet.

(Figure S2). For confirmation, we simulated the HAADF image (Figure 5b, inset) using the DFT-optimized interface structure (Figure 5a). A good correlation between the simulated and observed images was found, supporting the STM/STS observations.

To further confirm the species of the topmost TiO_2 nanomesh and to determine its valence state, we measured the electron energy-loss near-edge structure (ELNES) of the Ti-$L_{2,3}$ edge in the topmost layer (red), TiO_2 layer directly underneath the LaO layer (blue), and $SrTiO_3$ bulk (green) shown in Figure 6a. The ELNES signal of the Ti-$L_{2,3}$ edge was detected in the topmost nanomesh, which identifies it as TiO_2. Consequently, both the STEM (Figure 5b) and ELNES results (Figure 6a) clearly indicate that the Ti atoms reside on top of the $LaAlO_3$ layer. Moreover, a remarkable similarity is observed in the three ELNES spectra, which mainly comprise four peaks (two doublets), with the L_2 and L_3 edges at higher and lower energy losses, respectively. A clear split is visible for the L_2 and L_3 peaks, implying that the valence state of the Ti atoms in the topmost TiO_2 nanomesh was 4+. To corroborate this result, we measured the electrical resistance of the heterostructure, that is, 1-UC $LaAlO_3$ deposited on an insulating $SrTiO_3$(001)-($\sqrt{13}\times\sqrt{13}$)-*R*33.7° substrate, under high vacuum conditions, which prevented surface contamination. The sheet resistance was found to be on the order of GΩ/square, indicating that the Ti atoms of TiO_2 adopted a d^0 nature, which is consistent with the ELNES results. Thus, we successfully fabricated a single-atom-thick semiconducting TiO_2 nanomesh on an insulator (Figure 6b).

Considering the atomic arrangement of the single-atom-thick TiO_2 nanomesh on the $LaAlO_3/SrTiO_3$ and $SrTiO_3$(001)-($\sqrt{13}\times\sqrt{13}$)-*R*33.7° surfaces, the topmost Ti atoms must bond to the O atoms in the underlying AlO_2 layer. This forms truncated TiO_5 octahedra that can be stabilized by sharing their edges with the AlO_6 octahedra underneath, as schematically shown in Figure 1d. Hence, the periodic arrangement of O atoms in the AlO_2 layer acts as an anchor for the formation of a TiO_2 nanomesh. This structure suggests that the TiO_2 nanomesh can also be formed on (001)-oriented surfaces of other perovskites. To test this, we investigated $La_{0.7}Ca_{0.3}MnO_3$ ultrathin films,[27] which were determined to have a ($\sqrt{13}\times\sqrt{13}$) structure, corresponding to nanomeshes of TiO_2 or MnO_2. The results indicate that the formation of truncated octahedra in *TM*-O_5 structures is a common feature in the growth of complex TMO thin films on $SrTiO_3$(001)-($\sqrt{13}\times\sqrt{13}$)-*R*33.7° surfaces. These results indicate that the formation of nanomesh structure is universal on perovskite oxide surfaces, originating from the stability of truncated TiO_5 octahedra on these surfaces. That is, the stable formation of truncated TiO_5 octahedra on the surfaces is the driving force to form the TiO_2 nanomesh. Note that the TiO_2 2D nanomesh discussed here is vastly different from that reported by Sasaki *et al.*,[28,29] who showed that their $Ti_{0.87}O_2$ nanosheets prepared by the chemical exfoliation method had edge-linked TiO_6 octahedra in a lepidocrocite-type 2D lattice.

Understanding the growth process of the TiO_2 nanomesh at the atomic level is an important step toward further modifications of the physical and chemical properties of 2D structures. We speculate that the deposited La, Al, and O atoms first migrate on the $SrTiO_3$ reconstructed surface and to form an island, incorporating topmost Ti atoms on the surface of $SrTiO_3$, at the twin boundary of two ($\sqrt{13}\times\sqrt{13}$)-*R*33.7° reconstruction domains. Possibly, this island is amorphous upon formation, and then crystallizes to form $LaAlO_3$. During this process, excess Ti atoms are expelled to the $LaAlO_3$ surface, since the truncated TiO_5 octahedra on the surface is more stable than TiO_6 in $LaAlO_3$. We note that in many instances, $LaAlO_3$ islands nucleate at the twin boundary of two ($\sqrt{13}\times\sqrt{13}$)-*R*33.7° reconstruction domains. Nevertheless, no domain boundary is observed on the $LaAlO_3$ islands, and a single ($\sqrt{13}\times\sqrt{13}$)-*R*33.7° domain is always observed on the $LaAlO_3$ surface, justifying the hypothesis of the nucleation of the TiO_2 2D nanomesh on the $LaAlO_3$ *via* a mixture of La, Al, Ti, and O atoms. We believe the presence of truncated TiO_5 octahedra on the $LaAlO_3$ is not specific to the reconstructed $SrTiO_3$ surface. The stability of truncated TiO_5 octahedra should be significant even though the TiO_5

octahedra are randomly distributed over the $LaAlO_3$ surface.

CONCLUSIONS

We successfully synthesized a single-atom-thick TiO_2 2D nanomesh on an insulating $LaAlO_3/SrTiO_3$ heterostructure. The growth process indicates that the deposition of TiO_2 alone cannot create a TiO_2 nanomesh and that the $LaAlO_3$ deposition plays an essential role in the nanomesh formation. Furthermore, precise control of the oxide growth at the atomic scale was used to create the 2D nanomesh uniformly on other perovskite-oxide surfaces owing to the high stability of the truncated TiO_5 octahedra. The nanostructure can be potentially used to modify the physical and chemical properties of perovskite-oxide surfaces, and understanding the growth processes of oxide thin films will enable the discovery of new 2D nanostructures for a wide range of transition-metal oxides.

EXPERIMENTAL SECTION

Epitaxial Growth. Niobium-doped (0.1 atom %) $SrTiO_3(001)$ single crystals (Shinkosha Corp.) were used as substrates to ensure conductivity for low-temperature STM measurements. The substrates were etched in buffered HF and then annealed under an oxygen partial pressure of 1×10^{-5} Torr to produce $SrTiO_3(001)$-$(\sqrt{13}\times\sqrt{13})$-$R33.7°$ with step-and-terrace structures. The $SrTiO_3(001)$-$(\sqrt{13}\times\sqrt{13})$-$R33.7°$ surface reconstructions were confirmed using RHEED prior to the film growth. Epitaxial $LaAlO_3$ films were grown on the $SrTiO_3(001)$-$(\sqrt{13}\times\sqrt{13})$-$R33.7°$ substrates by PLD layer-by-layer under an oxygen partial pressure of 1×10^{-5} Torr at 800 °C, as previously reported by Nishimura *et al.*[30] The growth temperatures were controlled by direct-current resistive heating of the samples. Single-crystal $LaAlO_3$ targets were ablated by a KrF excimer laser (wavelength: 248 nm) at a repetition rate of 2 Hz with a laser fluence of 0.42 J/cm^2 at the $LaAlO_3$ target surface. The conductivity of a sample with a critical thickness of 4-UC was identical to that reported earlier.[31,32] After the growth, the samples were cooled to room temperature at a rate of 3−5 °C/s and immediately transferred to the STM chamber in a vacuum.

STM Measurements. All the STM/STS measurements were conducted at 4.2 K under ultrahigh vacuum conditions, and the STM images were obtained in a constant current mode. The coverage of the $LaAlO_3$ island formation was estimated according to the wide-scale STM images. In the LBH measurements, the distance (z) between the sample and probe tip was modulated with a peak-to-peak amplitude of 0.03 nm at a frequency of 197.3 Hz. The modulated component of the tunneling current was measured with a lock-in amplifier and converted to LBH using the formula $\Phi = 0.95 \times (\mathrm{d} \ln I/\mathrm{d}z)^2$, where Φ and z have units of eV and nm, respectively.[33] Prior to the LBH measurements, the tunneling current was confirmed to decay exponentially along the z direction, ensuring an ideal vacuum gap.

STEM Measurements. Specimens for STEM imaging were prepared by cutting, grinding, and dimpling the samples to a size of ∼20 μm. For the Ar ion-beam thinning process, we used a gun voltage of 1−4 kV and an incident beam angle of 4−6° to minimize the radiation damage to the samples. HAADF and ABF images were taken with a 200 kV ARM-200FC STEM that was equipped with a probe corrector (CEOS GmbH), providing an unprecedented opportunity to probe structures with sub-Ångstrom resolution. For the HAADF STEM imaging, a probe convergence angle of ∼22 mrad and a detector with an inner semiangle of over 60 mrad were used. The ELNES was recorded using a Gatan Enfina system built into the STEM with a full width at half-maximum (fwhm) energy resolution of ∼0.5 eV. The imaging simulations were based on the multislice method and employed the WinHREM program (HREM Research Inc.).

DFT Calculations. DFT calculations were performed using the STATE code,[34] with the plane-wave basis set and ultrasoft pseudopotentials.[35] We used the Wu−Cohen generalized gradient approximation[36] for the exchange-correlation functional. The system was modeled as a slab, and the artificial electrostatic interactions between periodic images[37] were eliminated using the effective screening medium method.[38] Computational details are provided in the Supporting Information.

Conflict of Interest: The authors declare no competing financial interest.

Acknowledgment. This study was supported by the World Premier Research Institute Initiative, promoted by the Ministry of Education, Culture, Sports, Science, and Technology of Japan (MEXT) for the Advanced Institute for Materials Research, Tohoku University, Japan. This work was also financially supported by Grants-in-Aid for Scientific Research (Kakenhi): Nos. 23686002, 22760021, and 26246022. T.O. acknowledges financial support from the Murata Foundation. Z.W. expresses thanks for financial support from a Grant-in-Aid for Young Scientists (A) (No. 24686069) and the NSFC (No. 11332013).

Supporting Information Available: The Supporting Information is available free of charge on the ACS Publications website at DOI: 10.1021/acsnano.5b02867.

Computational details (PDF)
Video demonstrating the similar spatial distribution of the LDOS between the $LaAlO_3$ island surface and the surrounding $SrTiO_3(001)$-$(\sqrt{13}\times\sqrt{13})$-$R33.7°$ surface (MPG)

REFERENCES AND NOTES

1. Chhowalla, M.; Shin, H. S.; Eda, G.; Li, L.-J.; Loh, K. P.; Zhang, H. The Chemistry of Two-Dimensional Layered Transition Metal Dichalcogenide Nanosheets. *Nat. Chem.* **2013**, *5*, 263–275.
2. Stojchevska, L.; Vaskivskyi, I.; Mertelj, T.; Kusar, P.; Svetin, D.; Brazovskii, S.; Mihailovic, D. Ultrafast Switching to a Stable Hidden Quantum State in an Electronic Crystal. *Science* **2014**, *344*, 177–180.
3. Wang, Q. H.; Kalantar-Zadeh, K.; Kis, A.; Coleman, J. N.; Strano, M. S. Electronics and Optoelectronics of Two-Dimensional Transition Metal Dichalcogenides. *Nat. Nanotechnol.* **2012**, *7*, 699–712.
4. Osada, M.; Sasaki, T. Two-Dimensional Dielectric Nanosheets: Novel Nanoelectronics From Nanocrystal Building Blocks. *Adv. Mater.* **2012**, *24*, 210–228.
5. Fukuda, K.; Ebina, Y.; Shibata, T.; Aizawa, T.; Nakai, I.; Sasaki, T. Unusual Crystallization Behaviors of Anatase Nanocrystallites from a Molecularly Thin Titania Nanosheet and its Stacked Forms: Increase in Nucleation Temperature and Oriented Growth. *J. Am. Chem. Soc.* **2007**, *129*, 202–209.
6. Sakai, N.; Ebina, Y.; Takada, K.; Sasaki, T. Electronic Band Structure of Titania Semiconductor Nanosheets Revealed by Electrochemical and Photoelectrochemical Studies. *J. Am. Chem. Soc.* **2004**, *126*, 5851–5858.
7. Hoffmann, M. R.; Hoffmann, M. R.; Martin, S. T.; Martin, S. T.; Choi, W.; Choi, W.; Bahnemannt, D. W.; Bahnemannt, D. W. Environmental Applications of Semiconductor Photocatalysis. *Chem. Rev.* **1995**, *95*, 69–96.
8. Tokura, Y., Ed. *Colossal Magnetoresistive Oxides*; Gordon and Breach Science Publishers: 2000.
9. Ogale, S., Ed. *Functional Metal Oxides: New Science and Novel Applications*; Wiley-VCH Verlag GmbH & Co. KGaA: 2013.
10. Bonaccorso, F.; Sun, Z.; Hasan, T.; Ferrari, A. C. Graphene Photonics and Optoelectronics. *Nat. Photonics* **2010**, *4*, 611–622.

11. Yazyev, O. V. Emergence of Magnetism in Graphene Materials and Nanostructures. *Rep. Prog. Phys.* **2010**, *73*, 056501.
12. Kasuga, T.; Hiramatsu, M.; Hoson, A.; Sekino, T.; Niihara, K. Formation of Titanium Oxide Nanotube. *Langmuir* **1998**, *14*, 3160–3163.
13. Iwaya, K.; Shimizu, R.; Hashizume, T.; Hitosugi, T. Systematic Analyses of Vibration Noise of a Vibration Isolation System for High-Resolution Scanning Tunneling Microscopes. *Rev. Sci. Instrum.* **2011**, *82*, 083702.
14. Iwaya, K.; Ohsawa, T.; Shimizu, R.; Hashizume, T.; Hitosugi, T. Atomically Resolved Surface Structure of $SrTiO_3$(001) Thin Films Grown in Step-Flow Mode by Pulsed Laser Deposition. *Appl. Phys. Express* **2010**, *3*, 075701.
15. Ohsawa, T.; Iwaya, K.; Shimizu, R.; Hashizume, T.; Hitosugi, T. Thickness-Dependent Local Surface Electronic Structures of Homoepitaxial $SrTiO_3$ Thin Films. *J. Appl. Phys.* **2010**, *108*, 073710.
16. Erdman, N.; Poeppelmeier, K. R.; Asta, M.; Warschkow, O.; Ellis, D. E.; Marks, L. D. The Structure and Chemistry of the TiO_2-Rich Surface of $SrTiO_3$(001). *Nature* **2002**, *419*, 55–58.
17. Kienzle, D. M.; Becerra-Toledo, a. E.; Marks, L. D. Vacant-Site Octahedral Tilings on $SrTiO_3$(001), The $SrTiO_3$(001)-($\sqrt{13}\times\sqrt{13}$)-*R*33.7° Surface, and Related Structures. *Phys. Rev. Lett.* **2011**, *106*, 176102.
18. Kienzle, D. M.; Marks, L. D. Surface Transmission Electron Diffraction for $SrTiO_3$ Surfaces. *CrystEngComm* **2012**, *14*, 7833–7839.
19. Hamada, I.; Shimizu, R.; Ohsawa, T.; Iwaya, K.; Hashizume, T.; Tsukada, M.; Akagi, K.; Hitosugi, T. Imaging the Evolution of *d* States at a Strontium Titanate Surface. *J. Am. Chem. Soc.* **2014**, *136*, 17201.
20. Shimizu, R.; Iwaya, K.; Ohsawa, T.; Shiraki, S.; Hasegawa, T.; Hashizume, T.; Hitosugi, T. Atomic-Scale Visualization of Initial Growth of Homoepitaxial $SrTiO_3$ Thin Film on an Atomically Ordered Substrate. *ACS Nano* **2011**, *5*, 7967–7971.
21. Shimizu, R.; Iwaya, K.; Ohsawa, T.; Shiraki, S.; Hasegawa, T.; Hashizume, T.; Hitosugi, T. Effect of Oxygen Deficiency on $SrTiO_3$(001) Surface Reconstructions. *Appl. Phys. Lett.* **2012**, *100*, 263106.
22. Ohsawa, T.; Shimizu, R.; Iwaya, K.; Hitosugi, T. Visualizing Atomistic Formation Process of SrO_x Thin Films on $SrTiO_3$. *ACS Nano* **2014**, *8*, 2223–2229.
23. Gariglio, S.; Reyren, N.; Caviglia, A. D.; Triscone, J.-M. Superconductivity at the $LaAlO_3/SrTiO_3$ Interface. *J. Phys.: Condens. Matter* **2009**, *21*, 164213.
24. Qiao, L.; Droubay, T. C.; Varga, T.; Bowden, M. E.; Shutthanandan, V.; Zhu, Z.; Kaspar, T. C.; Chambers, S. A. Epitaxial Growth, Structure, and Intermixing at the $LaAlO_3/SrTiO_3$ Interface As the Film Stoichiometry is Varied. *Phys. Rev. B* **2011**, *83*, 085408.
25. Hitosugi, T.; Shimizu, R.; Ohsawa, T.; Iwaya, K. Scanning Tunneling Microscopy/Spectroscopy on Perovskite Oxide Thin Films Deposited *In Situ*. *Chem. Rec.* **2014**, *14*, 935–943.
26. Pennycook, S. J.; Boatner, L. A. Chemically Sensitive Structure-Imaging with a Scanning Transmission Electron Microscope. *Nature* **1988**, *336*, 565–567.
27. Shimizu, R.; Ohsawa, T.; Iwaya, K.; Shiraki, S.; Hitosugi, T. Epitaxial Growth Process of $La_{0.7}Ca_{0.3}MnO_3$ Thin Films on $SrTiO_3$(001): Thickness-Dependent Inhomogeneity Caused by Excess Ti Atoms. *Cryst. Growth Des.* **2014**, *14*, 1555–1560.
28. Sasaki, T.; Watanabe, M. Osmotic Swelling to Exfoliation. Exceptionally High Degrees of Hydration of a Layered Titanate. *J. Am. Chem. Soc.* **1998**, *120*, 4682–4689.
29. Tanaka, T.; Ebina, Y.; Takada, K.; Kurashima, K.; Sasaki, T. Oversized Titania Nanosheet Crystallites Derived From Flux-Grown Layered Titanate Single Crystals. *Chem. Mater.* **2003**, *15*, 3564–3568.
30. Nishimura, J.; Ohtomo, A.; Ohkubo, A.; Murakami, Y.; Kawasaki, M. Controlled Carrier Generation at a Polarity-Discontinued Perovskite Heterointerface. *Japanese J. Appl. Physics, Part 2 Lett.* **2004**, *43*, L1032–L1034.
31. Ohtomo, A.; Hwang, H. Y. A High-Mobility Electron Gas at the $LaAlO_3/SrTiO_3$ Heterointerface. *Nature* **2004**, *427*, 423–426.
32. Thiel, S.; Hammerl, G.; Schmehl, A.; Schneider, C. W.; Mannhart, J. Tunable Quasi-Two-Dimensional Electron Gases in Oxide Heterostructures. *Science* **2006**, *313*, 1942–1945.
33. Wiesendanger, R. *Scanning Probe Microscopy and Spectroscopy Methods and Application*; Cambridge University Press: Cambridge, UK, 1994.
34. Morikawa, Y.; Ishii, H.; Seki, K. Theoretical Study of *n*-Alkane Adsorption on Metal Surfaces. *Phys. Rev. B* **2004**, *69*, 041403(R).
35. Vanderbilt, D. Soft Self-Consistent Pseudopotentials in a Generalized Eigenvalue Formalism. *Phys. Rev. B* **1990**, *41*, 7892–7895.
36. Wu, Z.; Cohen, R. E. More Accurate Generalized Gradient Approximation for Solids. *Phys. Rev. B* **2006**, *73*, 235116.
37. Hamada, I.; Otani, M.; Sugino, O.; Morikawa, Y. Green's Function Method for Elimination of the Spurious Multipole Interaction in the Surface/Interface Slab Model. *Phys. Rev. B* **2009**, *80*, 165411.
38. Otani, M.; Sugino, O. First-Principles Calculations of Charged Surfaces and Interfaces: A Plane-Wave Nonrepeated Slab Approach. *Phys. Rev. B* **2006**, *73*, 115407.